Preprints (www.preprints.org) | NOT PEER-REVIEWED | Posted: 9 May 2022 doi:10.20944/preprints202205.0096.v1

Article

Particle-based imaging tools revealing water flows in maize nodal vascular plexus

Ulyana S. Zubairova[1,2,3†‡*], Aleksandra Yu. Kravtsova [4‡], Aleksandr V. Romashchenko[1], Anastasiia A. Pushkareva[3], Alexey V. Doroshkov[1,3,5]

[1] Institute of Cytology and Genetics Siberian Branch, Russian Academy of Sciences, 630090, Novosibirsk, Russia; ulyanochka@bionet.nsc.ru (U.S.Z.); arom@bionet.nsc.ru (A.V.R.); ad@bionet.nsc.ru (A.V.D.)
[2] Institute of Computational Mathematics and Mathematical Geophysics Siberian Branch, Russian Academy of Sciences, 630090, Novosibirsk, Russia
[3] Novosibirsk State University, 630090, Novosibirsk, Russia; a.pushkareva@g.nsu.ru (A.A.P.);
[4] Kutateladze Institute of Thermophysics SB RAS, 630090, Novosibirsk, Russia; kravtsova.alya@gmail.com;
[5] Institute of Fundamental Biology and Biotechnology, Siberian Federal University, 660036, Krasnoyarsk, Russia
* Correspondence: ulyanochka@bionet.nsc.ru;
† Current address: Affiliation 1
‡ These authors contributed equally to this work.

Abstract: In plants, water flows are the major driving force behind the growth and play a crucial role in the life cycle. To study hydrodynamics, methods based on tracking small particles inside water flows occupy a special place. Due to these tools, it is possible to get information about the dynamics of the spatial distribution of the fluxes characteristics. In this paper, using contrast-enhanced MRI, we have shown that gadolinium chelate, used as an MRI contrast agent, marks the structural characteristics of xylem bundles of maize stem nodes and internodes. Supplementing MRI data, a high-precision visualization of xylem vessels by laser scanning microscopy was used to reveal structural and dimensional characteristics of the stem vascular system. In addition, we proposed the concept of using the prototype "Y-type xylem vascular bundles" as a model of the elementary connection of vessels within the vascular system. A Reynolds number can match the microchannel model with the real xylem vessels.

Keywords: plant 3D imaging; *Zea mays* L.; vascular system; internodes; nodal plexus; contrast-enhanced magnetic resonance imaging; laser scanning microscopy; lab-on-a-chip; particle image velocimetry; systems biology

1. Introduction

Plants are living hydrodynamic systems functioning through the movement of water, which is one of the fundamental factors of their homeostasis [1]. The plant water uptake system, a xylem, constitutes the part of the vascular tissue which is concerned with the transport of substances between root and shoot [2]. The major function of the xylem is to provide a low-resistance pathway for water from soil to the atmosphere through the plant roots, stems, and leaves [3]. Mainly plants transport water and dissolved minerals through xylem vessels composed of dead lignified cells [4].

The water transport system in vascular plants is very diverse and most often structurally complex. In the xylem, dead cells fulfil a transport (xylem vessels, tracheids) and mechanical support (fibres) role and cells which are alive and provide metabolic activity (xylem parenchyma) [2]. In most grasses, the xylem of the stem consists of nodes and internodes. The internodes comprise long axial bundles of the metaxylem and protoxylem vessels, while within the nodes they pass through a network of transverse bundles, and the metaxylem and protoxylem vessels connect by small tracheary elements. Only about 3% of axial vessels pass through nodes straightly. In those places where the axial vessels connect with the transverse vessels, various forms of vascular elements arise, often mediating by

© 2022 by the author(s). Distributed under a Creative Commons CC BY license.

Preprints (www.preprints.org) | NOT PEER-REVIEWED | Posted: 9 May 2022 doi:10.20944/preprints202205.0096.v1

three-way Y-type connections. Maize also has these features of vascular system topology [5–7].

Imaging-based plants physiology studying approaches provide the basis for many current and challenging tasks that require precise classification of objects based on analysis of many features. Tools for imaging water flows inside plant tissues could be very diverse, including, for example, raman imaging of water-transporting xylem vessels [8] or fast neutron tomography of root water uptake [9]. Certainly, magnetic resonance imaging (MRI) is a splendid technique for solving outstanding issues in plant science [10]. The study [11] dedicated MRI equipment and methods to study phloem and xylem transport in poplar, castor bean, tomato and tobacco. Micro-computed tomography allows three-dimensional visualisation revealing the spatial configuration and distribution of vascular bundles in maize stem [12–14]. In vivo MRI of xylem vessel contents in woody lianas [15], in the tomato peduncle [16], and in a cucumber plant in response to environmental changes [17] were also presented. In the study [18] synchrotron X-ray micro-imaging technique was employed to directly observe structural characteristics of xylem vessels in vascular bundles of excised maize leaves with high spatial resolution. [19] have presented a set of image-based pipelines to quantify maize stem images acquired using micro-computed tomography scanning technology, in this work maize stems of 20 maize cultivars and two growth stages were imaged using cicro-computed tomography scanning technology. In the study [20] 3D images of root-soil systems obtained by X-ray computed tomography are analysed to measure the porosity and the displacement fields in the soil located up to few cm from the maize root surface.

A combination of different methods, including confocal microscopy and X-ray micro-tomography revealed vascular architecture of the cauline system in Commelinaceae [21] and allowed to reconstruct a model of axial and radial transport of water in redundantly interconnected xylem vessels [22]. The work [23] established a new approach for combined MRI–PET measurement for plants, and to evaluate whether combined MRI–PET techniques have the potential to provide new insights into structural and functional traits of intact plants.

Although sap flow in the stem could be measured directly, for example in maize [24], for *in vivo* water distribution imaging, contrast-enhanced MRI is a promising approach. Paramagnetic compounds acting as a contrast are capable of influencing the T_1 or T_2 proton relaxation rates. Examples of such compounds are gadolinium chelates [25,26] and manganese salts. Relaxation behavior is associated with interactions between water and other cellular components [27]. Thus, different T_2 values reflect the different state of water in the materials, and higher T_2 values represent more mobile water, while lower values indicate that the water molecules are less mobile. The state of water and its mobility can be carried out according to T_2 information. The study [28] investigated the state of water in apple parenchyma tissue using paramagnetic ions (divalent manganese ions) and identified three water fractions in different cellular compartments: vacuole, cytoplasm, and cell wall/extracellular space. The study [29] observed three water fractions in broccoli and illustrated different interactions between the three water components and materials within broccoli tissues.

At the same time, the existing *in vivo* imaging tools for fluid transport do not reproduce accurate quantitative data on the interaction of flows within a plant vessels, while microfluidic devices could simulate transport processes in plants. Therefore developing lab-on-chip methods make it possible to reproduce the dynamics of the mechanism of liquid movement up the plant under conditions of a wide variation in vessel sizes. A synthetic tree-on-a-chip representing passive phloem loading and long-distance transport was presented in [30]. An artificial xylem chip representing 3D-printed vertical digital microfluidic platform was elaborated in [31]. Passive water ascent in a tall, scalable synthetic tree was showed in [32]. An artificial leaf to develop fluid pump driven by surface tension and evaporation was presented in [33]. Beside that computational fluid dynamic methods can be used to quantify the internal flow variables of xylem conducting vessels [34].

Preprints (www.preprints.org) | NOT PEER-REVIEWED | Posted: 9 May 2022 doi:10.20944/preprints202205.0096.v1

In this paper, we aimed to demonstrate a combination of imaging tools for water flow visualization in a case study of the maize stem vascular system. We used combined contrast-enhanced MRI, confocal laser microscopy, and a microfluidic chip modeling an element of vessels connection to determine structural features of the xylem transport on different levels.

2. Results

2.1. MRI approaches for water visualization inside the xylem vascular bundles system

Magnetic resonance imaging (MRI) is an attractive technique providing detailed, non-invasive and quantitative information about water transport and water balance within plant vascular system. For the stems of 8 week old maize plants, we have tested ultrahigh-field tomograph BioSpec 117/16 USR (Bruker, Germany, 11.7 T) as a tool for obtaining high-resolution images of water transport system structure and functioning. For a shoot region constructed by nested leaves, a set of images for different MRI modes were obtained. On a cross section, tissues with contrast water content are well visualized (Figure 1a–f).

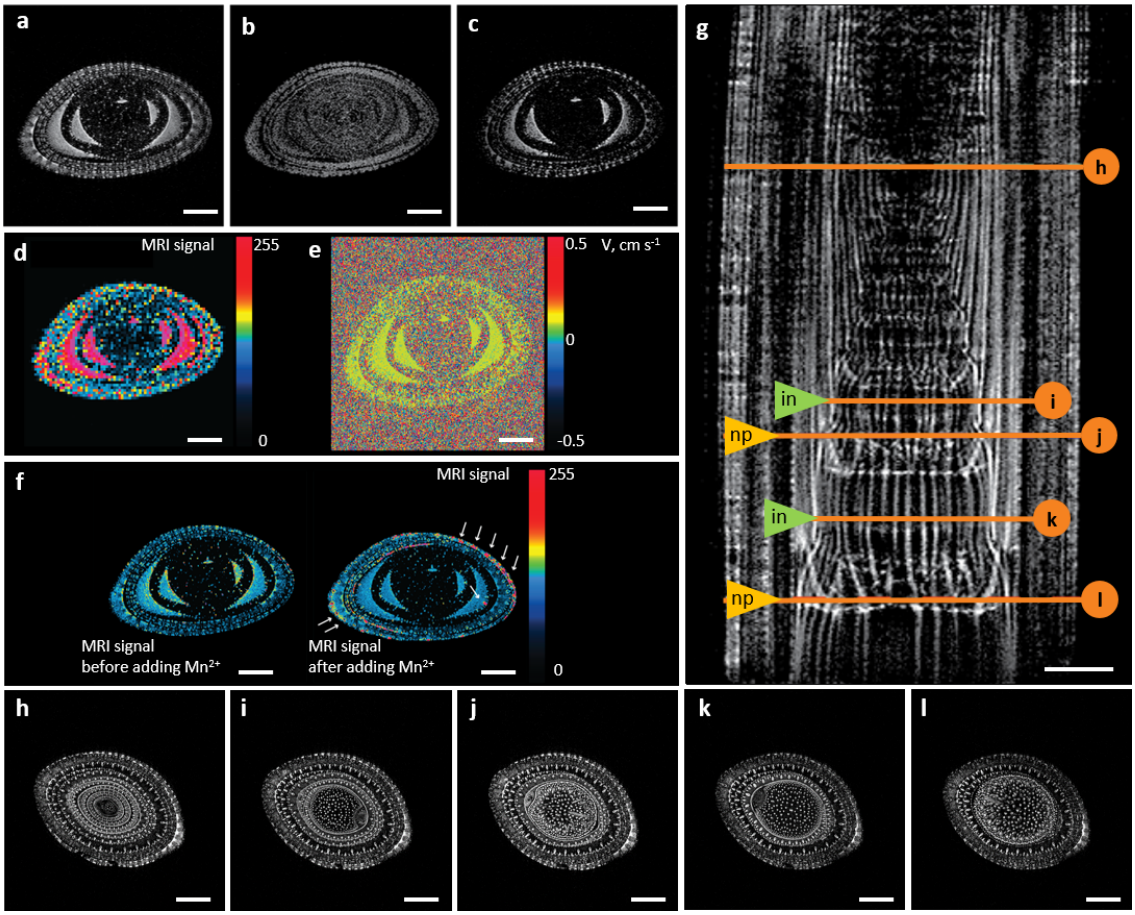

Figure 1. MRI methods for mapping the water distribution in the maize stem tissues: T_2-weighted MRI **(a)**; proton-weighted maps of non-aqueous **(b)** and aqueous **(c)** proton distributions; diffusion-weighted MRI **(d)** and velocity map of water flow through a virtual slice **(e)**. **(f)** T_1-weighted MRI before and after root exposure to $MnCl_2$ solution (10 mM). The arrows indicate the locations of manganese ions accumulation. Pseudo-staining reflects the intensity distribution of the MRI signal on the scan. MRI scans were axially oriented. **(g)** T_2-weighted MRI image of the growth zone of leaves and stem of maize. A longitudinal section of the stem **(g)** and some transverse sections **(h)–(l)** located in internodes **(i), (k)** and nodal plexus **(j), (l)** are shown. The pixel size is 56x56 μm, the slice thickness is 0.5 mm. Turbo Rapid Imaging with Refocused Echoes (TurboRARE) method.

Preprints (www.preprints.org) | NOT PEER-REVIEWED | Posted: 9 May 2022 doi:10.20944/preprints202205.0096.v1

Subtracting from each other T_1 and T_2-weighted images for the same object makes it possible to obtain proton-weighted (PD) maps for the distribution of aqueous and non-aqueous proton (polysaccharides, glycoproteins) showed for the maize stem in Figure 1a–c. In addition, images representing the diffusivity (Figure 1d) and flux can be obtained (Figure 1e).

Thus, for the vascular tissues of plants, horizontal tomograph Biospec 117/16 USR allows obtaining functional visualization representing a combination of anatomical and functional information. The use of T_1- and T_2-weighted sequences in comparison with diffusion- and proton-weighted methods made it possible to achieve higher resolution for visualization of the conducting system (Figure 1). The accumulation of Mn^{2+} in the plant tissue affects the relaxation time T_1 to a greater extent than T_2 (Figure 1f).

With T_2-weighted sequences, we have visualized structures of the conducting system for the maize stem (Figure 1g-l and Figure S1). On the longitudinal MRI section (Figure 1g), the vascular bundels of the stem, individual leaves, and nodes are distinguishable. It is interesting to note a well visualisation of highly contrastive topology of vascular bundles in nodal plexus (np) and internodes (in). Internodes contain parallel vessels without visible contacts between them. Whereas inside the nodes there are multiple vessel interconnections distributing water flows between the leaf of the corresponding stage and the distal part of the stem. Thus, each node contains elements of local topology complication including multiple branching and merging of conducting bundles of the vascular system. Despite the overall complexity of the system, an Y-type compound could be considered as an elementary unit.

Taking into account the conducted experimental imaging, in order to obtain information on the dynamics of water distribution over plant organs, we consider it promising to combine high-resolution T_2-weighted MRI and contrast-enhanced T_1-weighted MRI. As contrast agents, we use gadolinium chelate (see Section 2.2), which is not able to penetrate into cells and is located in the extracellular space, as well as manganese chloride, whose ions penetrate into the intracellular space through transporter proteins. Based on these data, it is possible to map the distribution of water in intra- and extracellular compartments.

2.2. Water flows in internodes and nodal plexus derived from contrast-enhanced MRI

Contrast-enhanced MRI may serve as a tool for imaging spatio-temporal water distribution features inside living tissues using contrast agents as a flow-markers. As a contrast agent we used gadolinium chelate, which once walked into the xylem vessel, cannot leave it due to its relatively large size. Note that in the nodal plexuses there are many narrow connections and locked vessels, where water passes by the transmembrane pathway. Internodes, on the contrary, consist of xylem vessels with a relatively large lumen. Therefore this experimental design allows to monitor the gadolinium chelate accumulation dynamics in the nodal plexus *in vivo* during extended period of time.

Preprints (www.preprints.org) | NOT PEER-REVIEWED | Posted: 9 May 2022 doi:10.20944/preprints202205.0096.v1

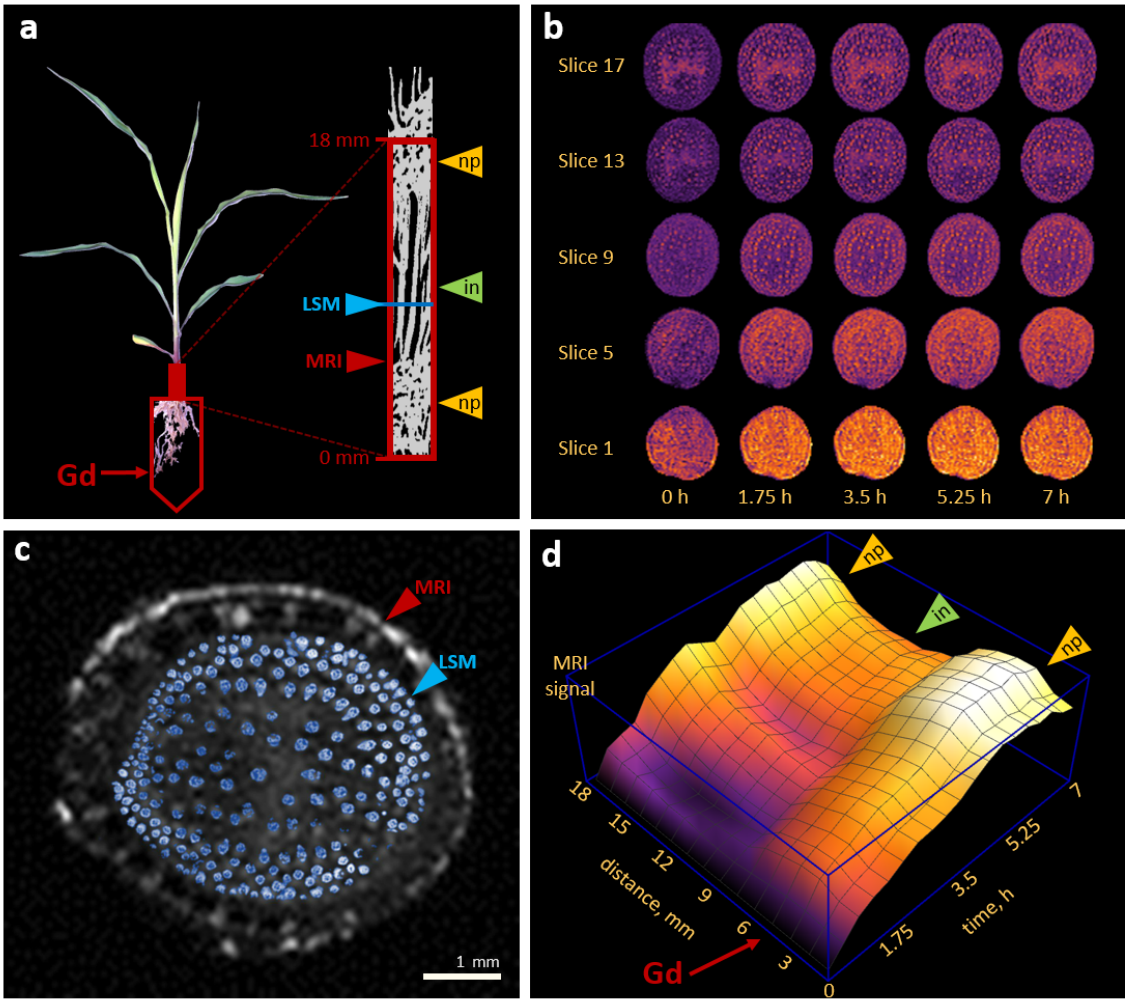

Figure 2. Contrast-enhanced MRI study of gadolinium chelate distributing inside nodal plexus (np) and internodes (in) of the maize stem. **(a)** The MRI-studied area marked by red arrow was located at the bottom of the maize stem directly from the root/shoot nodal plexus (np) and 18 mm higher. The location of the internode (in) section for high-resolution LSM-imaging is marked with a blue arrow. **(b)** Temporal serie of MRI slices. **(c)** Matching between internodal vascular bundles in the MRI slice and in the high-resolution LSM-image. **(d)** Spatial-time distribution for the MRI signal reflecting Gd penetration into maize stem xylem vascular system. The red arrow indicates the roots/stem connection region, which can be interpreted as a source of gadolinium chelate.

In the experiment we used a 4-week-old maize plant that had a small internode between the root-shoot and shoot apical nodal plexus. The MRI-studied area was located at the bottom of the stem and lasted directly from the junction of the shoot and root and 18 mm higher covering the bottom of the following node with shoot apical meristem and growing leaves (Figure 2a). After the roots were exposed to the contrast agent solution, scanning was performed every 23 minutes for 7 hours. This resulted in image series of spatio temporal signal distribution inside the stem (Figure 2b and Figure S2). Although the resolution of this imaging method allows only large vessels to be identified on images, the difference in the distribution pattern in nodal plexus (slices 1, 5, 17) and internodal (slice 9) regions. On the other hand laser scanning microscopy (LSM) provides high-resolution anatomical characteristics of xylem vessels incide vascular bundles (Figure 2c and Figure S3) complementing MRI. High-precision LSM-visualization of xylem vascular bundles was used to reveal structural and dimensional characteristics for the vessels, in particular for calculating the hydraulic diameters (D_h, see Section 2.4). The spatio-temporal distribution

Preprints (www.preprints.org) | NOT PEER-REVIEWED | Posted: 9 May 2022 doi:10.20944/preprints202205.0096.v1

of the signal averaged over the stem clearly shows areas of internodes that do not retain contrast agents, and areas of nodal plexuses that filter them and thereby accumulate the signal (Figure 2c).

2.3. Physical modeling of flows in microchannel prototype "Y-type xylem vascular connection"

The study of flow hydrodynamics was carried out on an experimental stand (Figure 3a) in the prototype "Y-type xylem vascular connection" (Figure 3d) with varying flow rates over a wide range. The minimum velocity value is comparable to the flow of water through the xylem vessels in the maize stem (the matching approach is outlined in the section 2.4). In the model experiment, the liquid (distilled water) flowed from two small vessels at velocities of Q_1 and Q_2, respectively, into one larger vessel. Several cases of ratio Q_2/Q_1 for flow rates were considered: 0.25, 0.5, and 1. For definiteness, the flow rate from the right channel was less than the flow rate from the left channel, except for the case of equal flow rates in both channels. Note that in the experiment for all considered ratios of input costs, their total consumption was equal, that is $Q_1 + Q_2 = Q = const$.

Preprints (www.preprints.org) | NOT PEER-REVIEWED | Posted: 9 May 2022 doi:10.20944/preprints202205.0096.v1

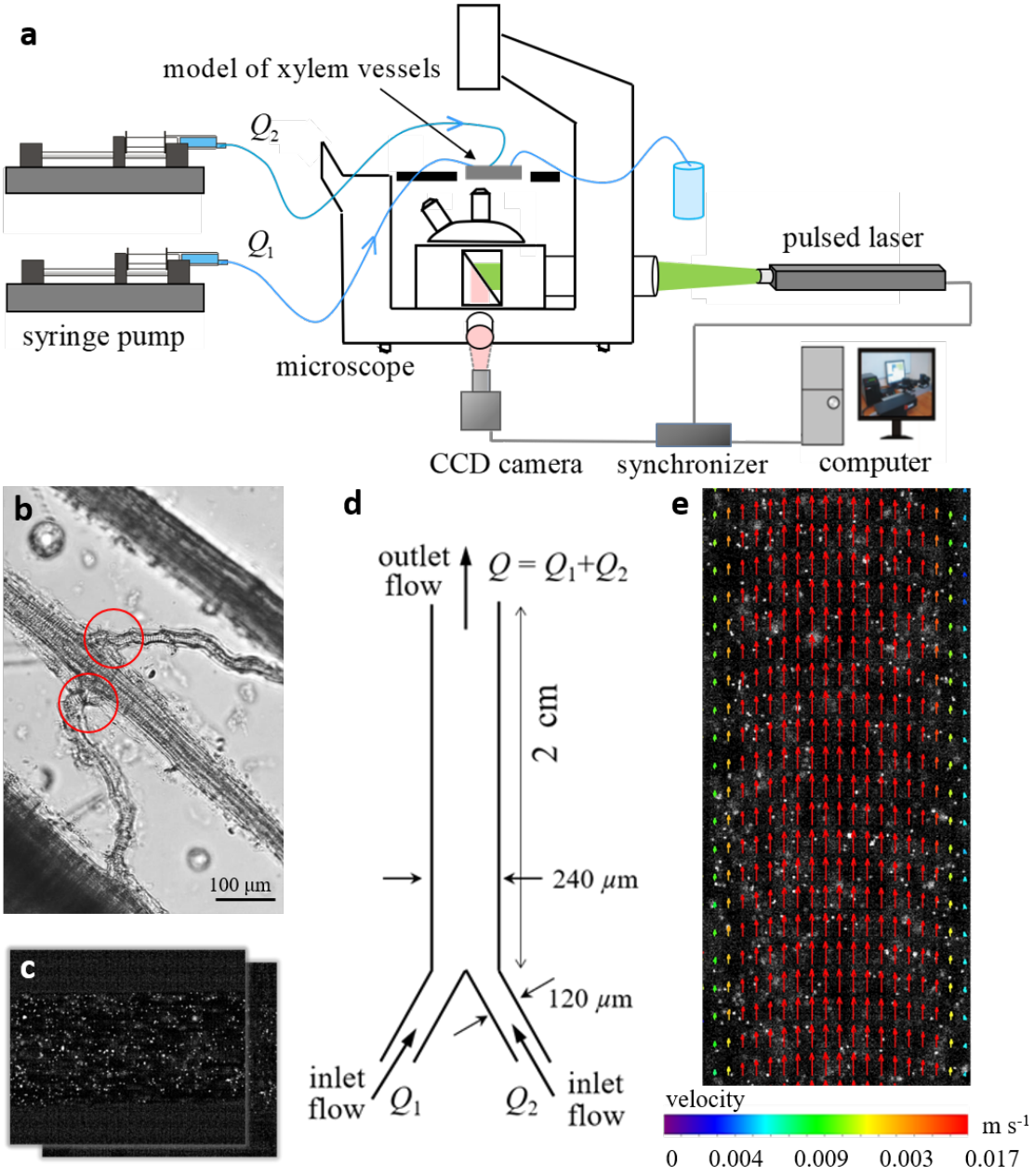

Figure 3. Particle Image Velocimetry. **(a)** General scheme of the experimental stand. **(b)** An example of a Y-type connection of xylem vessels (marked by red circules) in a maize leaf. The image of xylem vessels was obtained after 2 hours of enzymatic degradation of tissues in bright light on Olympus BX53 microscope (Olympus corporation, Japan) with 20x magnification. **(c)** Double image of tracer particles in a model microchannel. **(d)** Scheme of the prototype "Y-type xylem vascular connection". **(e)** Instantaneous velocity field obtained for double image superimposed on the tracer particles image.

With the value $Re = 3$ for all considered cases of ratios of the inlet flows velocities showed a laminar flow (Figure 4a). A decrease in the ratio for input costs leads to a shift in the maximum velocity component to one of the channel walls, which may affect the efficiency of water transport from xylem vessels to other tissues of the shoot.

Preprints (www.preprints.org) | NOT PEER-REVIEWED | Posted: 9 May 2022 doi:10.20944/preprints202205.0096.v1

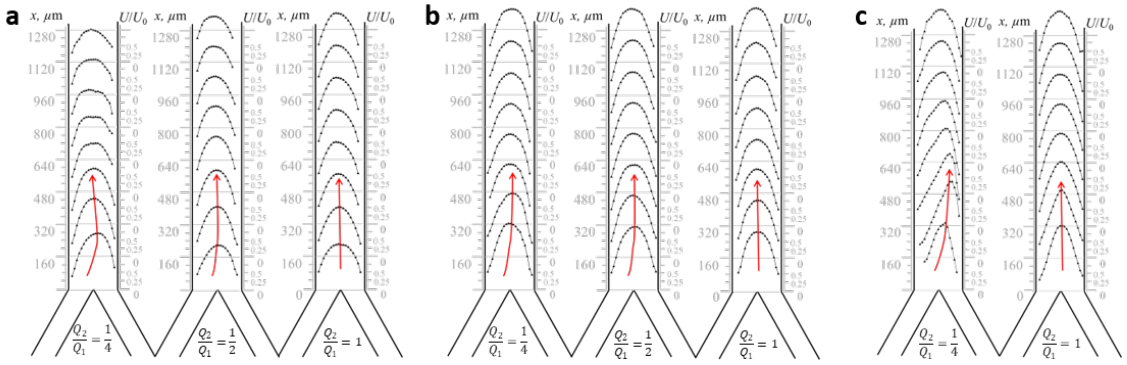

Figure 4. Longitudinal component of the average flow velocity in the prototype "Y-type xylem vascular connection" resulted from different ratios of inlet flow rates and equal total flow rate in the outlet channel. **(a)** $Re = 3$ equal to 0.1 mm per second; **(b)** $Re = 10$ equal to 0.25 mm per second; **(c)** $Re = 47$ equal to 1.2 mm per second.

Measurements were also made for the case of liquid flowing through the vessel at an average velocity of 0.25 mm per second (in dimensionless values, it corresponds to the number $Re = 10$). The ratio of input rates varied as well as for the case of $Re = 3$, but for $Re = 10$, with unequal input rates, the velocity profile is extended along the channel and the maximum value of the velocity increases by 0.25. This suggests that only due to the topology of the plexuses of microchannels it is possible to obtain significant variations in the spatial distribution of water flow velocities and predict hydraulic behaviour inside plant vascular system.

At higher water velocity in the plant (1.2 mm per second, $Re = 47$), it is possible to identify flow regions in which the velocity profile is significantly extended along the flow. There is a transverse mass transfer, which in turn can contribute to the formation of vortices inside the vessel.

2.4. Reynolds number-based matching between the xylem vessels in maize stem and microchannels in lab-on-a-chip

We observed the flow hydrodynamics in the prototype "Y-type xylem vascular bundles" for a wide range of velocities. On the other hand, for the model plant, we obtained LSM images for detailed structure reconstruction. In addition during the acquisition of a series of MRI-images, we fixed the volume of water that passed through the system of xylem vessels and evaporated through the leaves.

Since the plant grew under standard conditions of the growth chamber, and it was in dark during the study in the tomograph, we can assume that the liquid entered into xylem vessels evenly. Therefore, to estimate the average flow rate of fluid movement through the vessels in the section between two nodes, the following formula was used:

$$U_0 = \frac{Q}{S}, \tag{1}$$

where $U_0, m\ s^{-1}$ is mean flow velocity, $Q, m^3 s^{-1}$ is fluid flow through the plant, measured under experimental conditions, S, m^2 is the cross-sectional area of all xylem vessels of the plant, providing the movement of water from the root to the leaves. The total cross-sectional area of all xylem vessels was calculated as a result of the analysis of LSM images for the transverse section of the stem and amounted to 358292.39 μm^2 (see methodds in 4.2). Thus, the mean flow velocity of water through xylem vessels is $U_0 = 221.5$ μm s−1.

We used microfluidic chips to determine the features of fluid movement inside the vessels. Microfluidic chip configuration is described in section 4.4. The microchannels in the chip are usually larger than the actual vessel in the plant, that allows to use the modern methods of imaging diagnostics for flows with high spatial and temporal resolution [35], and to obtain spatial quantitative characteristics of pressure, velocity, diffusion for the

Preprints (www.preprints.org) | NOT PEER-REVIEWED | Posted: 9 May 2022 doi:10.20944/preprints202205.0096.v1

flow inside the microchannel. The data obtained in the experiment for the spatial velocity distributions are shown in the Figure 4.

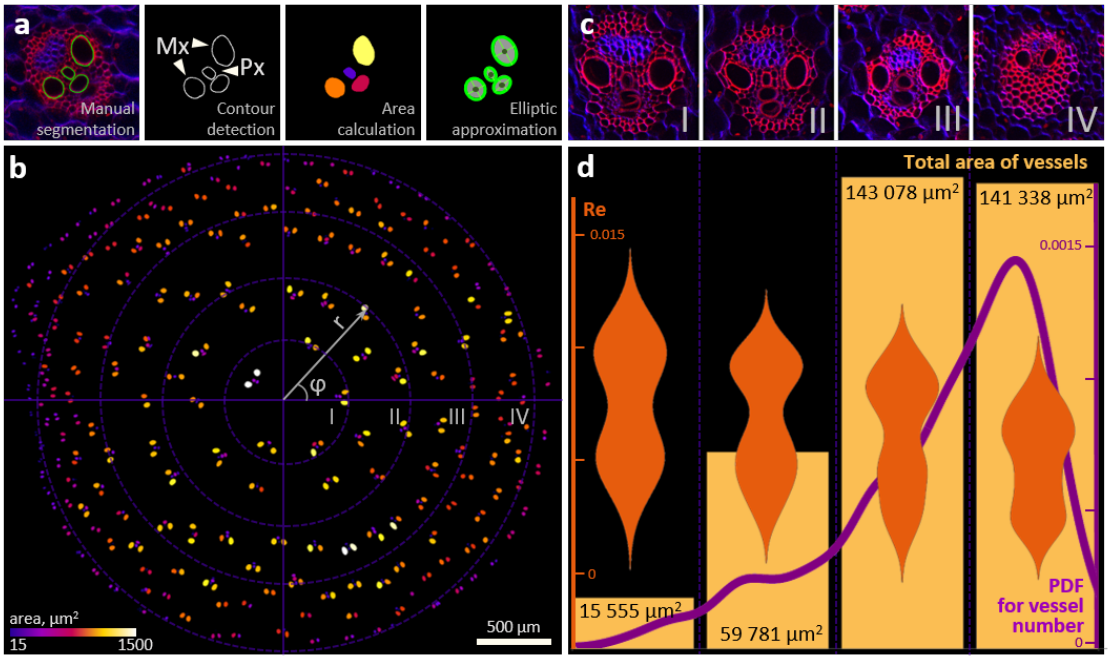

Figure 5. LSM image-based determination of numerical characteristics for Reynolds number-based matching between the xylem vessels in the maize stem and microchannels in lab-on-a-chip model. **(a)** The main stages of LSM image processing for obtaining data on the spatial distribution of the dimensional characteristics of the xylem vessels (metaxylem, Mx, and protoxylem, Px) in the internode of the maize stem, including expert manual segmentation, contour extraction, calculation of cross-sectional areas and ellipse fitting. **(b)** The location of the xylem vessels on the cross section of the maize stem in the I, II, III, or IV "ring", the coordinates are recalculated into the polar system relative to the nominal center of the stem, the color indicates the cross section of the vessel area. **(c)** LSM images for typical xylem bundles located in the I, II, III, and IV "rings". **(d)** For xylem bundles located in the I, II, III, and IV "rings", the distribution of vessels relative to the center of the stem, the total cross-sectional areas, violin plots for Reynolds numbers (*Re*).

The data presented in Figure 4 qualitatively show the features of fluid movement through the vessels. To quantitatively compare fluid motion in real xylem vessels and a model chip, we will use the following approach. The Reynolds number (*Re*) is a similarity criterion in micro, mini- and macro-dimensions and characterizes the ratio of the inertia forces acting in the flow to the viscous forces.

$$Re = \frac{U_0 D_h}{\nu}, \tag{2}$$

where U_0, $m\ s^{-1}$ is mean flow velocity, D_h, m is characteristic vessel size, ν, $m^2\ s^{-1}$ is kinematic viscosity. In the experiment, distilled water with dissolved particles of gadolinium chelate was presented to the plant roots, the water temperature was 26°C, the kinematic viscosity was $\nu = 8.74 \cdot 10^{-7}\ m^2\ s^{-1}$. Since xylem vessels in cross section are close in shape to ellipses (see Figure 5), then its hydraulic diameter D_h could be taken as the characteristic size of the vessel.

$$D_h = \frac{4S}{P}, \tag{3}$$

For the studied plant, the D_h value for the vessels varies between 3.8 μm and 46 μm. Then, the Reynolds number calculated by the formula (2) varies from 0.001 to 0.012 (Figure 5 and Supplementary table S4).

Preprints (www.preprints.org) | NOT PEER-REVIEWED | Posted: 9 May 2022 doi:10.20944/preprints202205.0096.v1

Thus, the obtained values of the Reynolds number are quite low, and for a quantitative comparison of the velocity characteristics of the liquid inside the microfluidic chip and the plant vessels, it is worth considering the flows at equal Reynolds numbers.

3. Discussion

In this work we have demonstrated the use of the horizontal tomograph Biospec 117/16 USR with a magnetic field strength of 11.7 T as a tool that allows you to visualize maize vascular system with high accuracy. The resulting images showed a complex topology for the connections of xylem bundles, which is consistent with data obtained by other methods [5,6]. The basis for nuclear magnetic resonance imaging is based on the following principles. Water molecules contain two protons. In a strong magnetic field, the alignment of the magnetic moments of the spin-bearing elements leads to a weak magnetization of the sample, which we can manipulate by applying time-dependent magnetic field pulses at the appropriate frequency (radio or high frequency pulses). The magnetization component of the sample perpendicular to the main magnetic field induces a slight inductive voltage in the detector coil of radius r placed around the sample. The frequency components of the time dependent inductive signal can be analyzed using a Fourier transform resulting in a frequency spectrum. In a uniform magnetic field B_0, identical spins (for example, protons of water molecules) have the same Larmor precession frequency or resonant frequency, and a single resonant line is observed in the frequency spectrum. Inside the magnet, a well-defined constant magnetic field gradient G is created, $G = \frac{\partial B_0}{\partial r}$, so identical spins at different positions along this gradient have different resonant frequencies because the resonant frequency is proportional to the local magnetic field experienced. The spins can be oriented in three independent x, y, or z directions, or its combinations, and therefore can be uniquely spatially encoded. Spin positions mapping by magnetic field gradients can be done in various ways [36]. Depending on the radiofrequency sequence used to excite the spins, the signal intensity in MRI images depends to a greater or lesser extent on a combination of parameters that reflect the spin density: relaxation time T_1 (spin-lattice) or T_2 (spin-spin). In addition to these parameters, the diffusion behavior of the molecules can also contribute to the contrast [37]. Regarding the use of MRI to determine the flow of water and solutions in the vascular system of a plant, it should be noted that in publications known to us MRI was used to determine the flow of water in the vascular system of plant stems [38,39]. This is because of the fairly high speed of convective flow in the stem vessels, which determines the successful application of MRI.

Contrast-enhanced MRI demonstrated in the current study is a promising tool for obtaining data on water content inside a plant tissues with high time and spatial resolution. Such data could be used to discriminate between the convective and diffusion components of flows in a framework of models of plant tissue hydraulics [40] to clarify mechanisms on the water pathways [41].

A brief discussion is warranted regarding the differences between natural xylem bundles and our microfluidic model. We studied the features of the movement of the fluid necessary for growth, nutrition, photosynthesis, which occurs upward inside the plant from roots to leaves along the complex structure of xylem bundles, by assessing the hydrodynamics of the flow within the microfluids system. In a system that implements the so-called lab-on-a-chip approach, which models the connecting element of a conducting system consisting of alternating blocks of transverse nodal plexuses and longitudinal axial filaments, the inlet flows were regulated and varied (Figure 3a). Experimental systems designed to simulate transport processes in plants have been developed by several authors [30,42,43].

Plant xylem bundles play an important role as interfaces between roots, stems and leaves. The description of the features of the movement of liquids through the vascular bundles after the nodes, depending on the input parameters, greatly contributes to the understanding of the transport of assimilates and minerals in plants. Non-contact field measurement methods with micron resolution are best suited for studying these processes. One

Preprints (www.preprints.org) | NOT PEER-REVIEWED | Posted: 9 May 2022 doi:10.20944/preprints202205.0096.v1

of the most modern and effective methods for studying hydrodynamics in a microfluidics chip is the micro Particle Image Velocimetry (micro-PIV). The method was proposed in 1998 by J.G. Santiago and C.D. Meinhart based on the PIV method for studying instantaneous and average velocity fields in liquid, gas and flame. This method is based on the calculation of the movement of particles (tracers) in the flow section for a certain time interval. The micro-PIV method makes it possible to measure velocity vector fields in channels with micron resolution, while retaining the main advantages of the PIV method, such as non-contact and wide dynamic range. Hoffmann et al. pioneered these methods to study liquid-liquid flows in a T-channel by performing imaging and quantifying mixing efficiency by defining a concentration field [44]. The improvement of the measurement method was achieved in the works [45,46]. However, for many years the error in determining the speed characteristics remained quite high. This problem was overcome in the work [35] and was also applied in this study. To calculate the velocity vectors, cells extended along the flow were used, which made it possible to achieve a relatively large dynamic range (the span between the maximum and minimum velocity). Inaccuracy of the offset determination does not exceed 0.1 pixel. Thus, the error of the method for measuring the average flow rate decreased to 1%.

The laminar flow of liquid in a tube is known to be observed at low flow rates, in other words Poiseuille flow occurs. The velocity profile becomes elongated along the flow direction and is approximated by a polynomial of the second degree. The double lengthening of the polynomial in the case where the velocity maximum is observed at values close to $2U_0$ (see Figure 4) is a feature of ultra-slow flows that are typically found in plant vessels. At the same time, small changes in the velocity profile with different inflow of liquid into the tube are observed. So, if the flow moves evenly across the entire width, then the velocity profile is symmetrical with respect to the center of the channel; and the maximum value of the velocity is reached in its central part. When liquid enters the channel unevenly, the velocity profile shifts to one of the channel walls and, as a rule, an increase in the maximum velocity value in the initial section of the microchannel is observed. After the liquid has passed about 1 mm of the path, the velocity profile again becomes symmetrical about the central part of the channel. However, in the plant vascular system, there are regions with more frequent connections than ones necessary for hydraulic signal fading. Such mutual influence for fluxes could modify the behavior of the entire system and underlay the mechanism of self-regulation.

Thus, the use of lab-on-chip methods together with the possibility of non-invasive measurement methods can provide a new frontiers in the study of the movement of microscale fluid through plant vessels. With the ability to vary and maintain flow inputs such as pressure and velocity, and external factors such as ambient temperature and moisture content, the lab-on-a-chip can operate at steady state for many hours, allowing accurate measurements of dynamic processes within the system.

4. Materials and Methods

4.1. Plant material

Maize (*Zea mays* L.) variety B73 was used as an experimental plant for testing visualization tools. Plant samples were hydroponically grown in an environment-controlled growth chamber at 26°C and 70% relative humidity, with 12 h of daily illumination (600 μmol m^{-2} s^{-1}).

4.2. Laser scanning microscopy (LSM)

The studied stem samples were prepared for microscopy by the following procedure. We incubated the tissues in fixative solution 3:1 (ethanol:acetic acid) for three or more hours. The section of the stem between the two nodes was sliced at 200 µm sections. Staining was done with fluorescent dyes 4',6-diamidino-2-phenylindole (DAPI, Sigma-Aldrich, Burlington, MA, United States) and Propidium Iodide (PI, Sigma-Aldrich). This set of dyes on a fixed material provides a fairly fade-resistant staining of nuclei and cell walls,

Preprints (www.preprints.org) | NOT PEER-REVIEWED | Posted: 9 May 2022 doi:10.20944/preprints202205.0096.v1

including the vessels of the conducting system. Staining was carried out in two stages, with intermediate washing with neutral phosphate buffer. Leaf fragments washed twice were placed in a 10 µg/mL of PI solution for 30 min, then washed again twice for 15 min. Next, the fragments were stained with a 10 µg/mL DAPI solution for 30 min and placed under a coverslip. The DABCO reagent (Sigma-Aldrich) was used as an antifade, which made it possible to carry out prolonged microscopic analysis in the future. DABCO was diluted according to the standard procedure (25 mg/ml DABCO in 90% glycerol, 10% 1 × PBS pH = 8.6). This mounting solution had sufficient viscosity to hold the coverslip on the sample fragment.

The stained samples of stem cross sections were imaged with LSM 780 NLO microscope (Zeiss, Germany) using objective Plan-Apochromat 20x/0.8 M27 in the "tile scan" mode with 6 µm distance between adjacent optical sections along the vertical axis. The signal amplification was chosen dynamically. The pixel size on the optical sections was 0.692x0.692 µm. As the result we obtained 2-channel 3D images for an extended region containing the whole stem in high resolution.

Tiles of 3D images were assembled into a single 3D-image using the plugin LSM-W^2 (ICG SB RAS, Novosibirsk, Russia, https://imagej.net/plugins/lsm-worker, accessed on 23 April 2022, [47]), then the built-in functions of Fiji (https://fiji.sc/, accessed on 23 April 2022) for maximum intensity projection of the both channels converted the image to 2D.

Segmentation for evaluation of the structural characteristics of the vascular system was performed manually by an expert. In the separate channel, xylem bundles and individual vessels were highlighted. Using the built-in functions of Fiji (https://fiji.sc/ accessed on 23 April 2022) Image > Color > Split Channels as well as functions from MorphoLibJ (http://imagej.net/MorphoLibJ accessed on 23 April 2022, [48]), Plugins > MorphoLibJ > Segmentation > Morphological Segmentation we have got the data on dimensional and spatial distribution characteristics for individual vessels (Suoolementary Table S4).

4.3. Magnetic Resonance Imaging

Images were acquired on a horizontal tomograph Biospec 117/16 USR (Bruker BioSpin, Ettlingen, Germany) with a magnetic field strength of 11.7 T.

As a contrast agent Gadolinium-DTPA-BMA (Gadolinium 5,8-bis(carboxylatomethyl)-11-[2-(methylamino)-2-oxoethyl]-3-oxo-2,5,8,11-tetraazatridecan-13-oate) [49] was used. The studied area was located in the bottom part of the maize shoot, starting from the junction between the root and stem and was 18 mm. The area was scanned in two successive 9 mm series. As a reference, a test tube with distilled water was placed next to the plant. The distance between slices was 1 mm, each slice averaged information about 750 µm along the growth axis. This area was scanned by equal intervals during 7 hours. The studied plant was not removed from the tomograph until the end of the experiment. Thus, we have obtained a spatio-temporal series of slices for a maize stem. All the images were exported as dicom files in the ParaVision 5.1 Software (Bruker, Ettlingen, Germany).

On each image, areas corresponding to a stem, a test tube with water, and air were segmented. For each of these segments, the mean pixel intensity values were calculated. To take into account the noise in the data, the final value that determines the flow of water with gadolinium was calculated using the following formula:

$$S(flow_i^t) = \frac{S(stem_i^t) - S(stem_i^0)}{S(air_i^t)}, \tag{4}$$

where X_i^t is the region on the image $i \in \{1, \dots 18\}$, in the time moment $t \in \{1, \dots, 19\}$, $S(X_i^t)$ is mean value of pixel intensity in the area X_i^t. The values according to Formula (4) were calculated for each slice at each time point. The resulting distribution is shown in Figure 2d.

Preprints (www.preprints.org) | NOT PEER-REVIEWED | Posted: 9 May 2022 doi:10.20944/preprints202205.0096.v1

4.4. Particle Image Velocimetry

An experimental study of the hydrodynamic characteristics of fluid flow in microchannels was carried out on a unique scientific facility of the Institute of Thermophysics of the Siberian Branch of the Russian Academy of Sciences. The experimental stand includes a syringe pump (Gemini 88 Plus Dual Rate Syringe Pump, KD Scientific), a working area, a microscope (Carl Zeiss Axio Observer.Z1, Germany), and a measuring system Particle Image Velocimetry (Novosibirsk, Russia). The work [50] contains a detailed description of the facility design.

Measurements of the velocity characteristics of the flow were carried out in a microfluidic chip with two inlets connected to each other at an angle of 60 degrees and one outlet (Figure 3d). The inlet channels have a square section with a side equal to 120 μm, the outlet channel has a rectangular section 120x240 μm. The aspect ratio is 1:1:2. The length of the inlet sections is 0.7 cm, the length of the outlet section is 2 cm. The channel walls are made of optically transparent material SU-8 (microLIQUID, Mondragon, Spain). Irregularities on the channel walls do not exceed 20 μm. The syringe pump provides a continuous supply of fluid to the microchannel inlets. The fluid flow rate at the inlets varies from 0.39 ml/hour to 115 ml/hour. Distilled water was used in the experiment as the working fluid. The Reynolds number (Re) varied from 3 to 100.

For definiteness, we assume that the input flow rate on the right channel is less than or equal to the flow rate on the left one ($Q_2 \leq Q_1$), and their sum is constant in all cases ($Q_1 + Q_2 = Q$). The ratio of input costs is expressed by the coefficient $R = Q_2/Q_1$.

The velocity characteristics of the currents were measured by Particle Image Velocimetry (PIV) method with micron resolution, using a double pulsed Neodymium:Yttrium-Aluminum-Garnet laser (radiation wavelength 532 nm, pulse repetition rate 4 Hz, pulse duration 10 ns, pulse energy 25 mJ), CCD-camera (depth 8 bits, matrix resolution 2048x2048 pixels), and a synchronizing processor (Figure 3a). The spatial resolution was 1 μm per pixel. The measuring system was controlled by software package ActualFlow (Russia, Novosibirsk, http://polis-instruments.ru/). To carry out PIV measurements, fluorescent 2 μm tracer particles (red fluorescent polymer microspheres, Rhodamine 6G, Thermo Fisher Scientific, USA) were added to the flow (Figure 3c).

We obtained 5000 images for each flow regime, which made it possible to minimize the measurement error of the velocity fields [51]. An iterative cross-correlation algorithm with continuous displacement and deformation of elementary computational domains and 50% overlap between them was used to calculate velocity fields. Sub-pixel interpolation of the cross-correlation peak was carried out on three points, using a one-dimensional Gaussian approximation. In order to have a relatively large dynamic range, the size of the initial computational area corresponded to 128×32 pixels. The size of the final computational area was 32×8 pixels to provide a relatively high spatial resolution. The error for determining the offset did not exceed 0.1 pixel. Thus, when the tracers were shifted by 8 and 2 pixels, the velocity measurement error was 1% and 4%, respectively. Validation of the calculated velocity vectors took place in two stages: validation by the signal-to-noise ratio with a threshold of 2, adaptive median filtering with a region size of 7x7. An example of the obtained instantaneous velocity field is shown in Figure 3e. At the next step, we averaged the instantaneous velocity fields and obtained the field of the average current velocity of the measurement area. Based on the average current velocity fields, the velocity profiles were constructed.

5. Conclusions

Modern imaging techniques make it possible to study the plants' functioning features at different levels from the ultrastructure of cells and tissues to the organization of plant communities. Systems biology approach allows integrating these levels into complete model water flows through soil-plant-atmosphere continuum. The most significant outcomes can be obtained as a result of assembling of approaches at different levels. This paper showed a way for a combination of imaging tools for water flow visualization inside the

Preprints (www.preprints.org) | NOT PEER-REVIEWED | Posted: 9 May 2022 doi:10.20944/preprints202205.0096.v1

maize stem vascular system including contrast-enhanced MRI, laser scanning microscopy, and a microfluidic chip modeling an element of vessels connection. For the resulted images, the pixel sizes differed by two orders of magnitude. We believe that new peculiarities of plant vascular system functioning could emerge from a suchlike comprehensive and quantitative consideration of the many determinants of water flow within the plant vascular system.

Supplementary Materials: The following are available online at https://www.mdpi.com/article/10.3390/plants1010000/s1, Figure S1: T2-weighted MRI 3D image of a maize stem, Figure S2: Spatio-temporal series of MRI images of a maise stem depicting the change in signal distribution caused by the penetration of gadolinium chelate into xylem vessels, Figure S3: LSM image of a cross section of the maize stem internode, Table S4: Parameters for transverse sections of xylem vessels based on LSM image analysis.

Author Contributions: Conceptualization, U.S.Z., A.V.D. and A.Yu.K.; methodology, U.S.Z., A.V.D., A.V.R. and A.Yu.K.; formal analysis, U.S.Z., A.V.R., A.A.P., A.V.D., and A.Yu.K.; writing—original draft preparation, U.S.Z., A.V.R., A.A.P., A.V.D., and A.Yu.K.; writing—review and editing, U.S.Z., A.V.R., A.V.D., and A.Yu.K.; visualization, U.S.Z., A.V.R., A.V.D., and A.Yu.K.; funding acquisition, U.S.Z. and A.Yu.K. All authors have read and agreed to the published version of the manuscript.

Funding: The MRI and LSM studies in a plant was funded by RSF grant number 19-74-10037. The study of water flows in microchannels was funded by by RSF grant number 19-79-10217. The APC was equivalently funded by RSF grant number 19-74-10037 and RSF grant number 19-79-10217.

Institutional Review Board Statement: Not applicable.

Informed Consent Statement: Not applicable.

Acknowledgments: Plant cultivation was conducted in the ICG Joint Center for Plant reproduction. LSM imaging was performed at the Joint Access Center for Microscopy of Biological Objects of the Institute of Cytology and Genetics SB RAS. The authors thank the researchers of Siberian Federal University for fruitful discussions of the results presented in the article, as well as the Institute of Computational Mathematics and Mathematical Geophysics SB RAS for providing resources and software for calculations.

Conflicts of Interest: The authors declare no conflict of interest.

Abbreviations

The following abbreviations are used in this manuscript:

MRI	Magnetic Resonance Imaging
LSM	Laser Scanning Microscopy
PI	Propidium iodide
DAPI	4′,6-diamidino-2-phenylindole
PIV	Particle Image Velocimetry
micro-PIV	micro Particle Image Velocimetry
Re	Reynolds number

References

1. Lucas, W.J.; Groover, A.; Lichtenberger, R.; Furuta, K.; Yadav, S.R.; Helariutta, Y.; He, X.Q.; Fukuda, H.; Kang, J.; Brady, S.M.; et al. The plant vascular system: evolution, development and functions f. *Journal of integrative plant biology* **2013**, *55*, 294–388. doi:10.1111/jipb.12041.
2. Fricke, W. Xylem: Differentiation, Water Transport and Ecology. *eLS* **2017**, pp. 1–7. doi:10.1002/9780470015902.a0002076.pub2.
3. Lobet, G.; Couvreur, V.; Meunier, F.; Javaux, M.; Draye, X. Plant water uptake in drying soils. *Plant physiology* **2014**, *164*, 1619–1627. doi:10.1104/pp.113.233486.
4. Holbrook, N.M.; Zwieniecki, M.A.; Melcher, P.J. The dynamics of "dead wood": Maintenance of water transport through plant stems. *Integrative and Comparative Biology* **2002**, *42*, 492–496. doi:10.1093/icb/42.3.492.
5. Shane, M.; McCully, M.E.; Canny, M. The vascular system of maize stems revisited: implications for water transport and xylem safety. *Annals of Botany* **2000**, *86*, 245–258. doi:10.1006/anbo.2000.1171.

Preprints (www.preprints.org) | NOT PEER-REVIEWED | Posted: 9 May 2022 doi:10.20944/preprints202205.0096.v1

6. Shane, M.; Cully, M.M.; Canny, M. Architecture of branch-root junctions in maize: structure of the connecting xylem and the porosity of pit membranes. *Annals of Botany* **2000**, *85*, 613–624. doi:10.1006/anbo.2000.1113.
7. Kraehmer, H. On vascular bundle modifications in nodes and internodes of selected grass species. *Scientia agriculturae bohemica* **2017**, *48*, 112–121. doi:10.1515/sab-2017-0018.
8. Pascut, F.C.; Couvreur, V.; Dietrich, D.; Leftley, N.; Reyt, G.; Boursiac, Y.; Calvo-Polanco, M.; Casimiro, I.; Maurel, C.; Salt, D.E.; et al. Non-invasive hydrodynamic imaging in plant roots at cellular resolution. *Nature Communications* **2021**, *12*, 1–7. doi:10.1038/s41467-021-24913-z.
9. Tötzke, C.; Kardjilov, N.; Hilger, A.; Rudolph-Mohr, N.; Manke, I.; Oswald, S.E. Three-dimensional in vivo analysis of water uptake and translocation in maize roots by fast neutron tomography. *Scientific reports* **2021**, *11*, 1–10. doi:10.1038/s41598-021-90062-4.
10. Borisjuk, L.; Rolletschek, H.; Neuberger, T. Surveying the plant's world by magnetic resonance imaging. *The Plant Journal* **2012**, *70*, 129–146. doi:10.1111/j.1365-313X.2012.04927.x.
11. Windt, C.W.; Vergeldt, F.J.; De Jager, P.A.; Van As, H. MRI of long-distance water transport: a comparison of the phloem and xylem flow characteristics and dynamics in poplar, castor bean, tomato and tobacco. *Plant, Cell & Environment* **2006**, *29*, 1715–1729. doi:10.1111/j.1365-3040.2006.01544.x.
12. Du, J.; Zhang, Y.; Guo, X.; Ma, L.; Shao, M.; Pan, X.; Zhao, C. Micron-scale phenotyping quantification and three-dimensional microstructure reconstruction of vascular bundles within maize stalks based on micro-CT scanning. *Functional Plant Biology* **2016**, *44*, 10–22. doi:10.1071/FP16117.
13. Zhang, Y.; Ma, L.; Pan, X.; Wang, J.; Guo, X.; Du, J. Micron-scale phenotyping techniques of maize vascular bundles based on X-ray microcomputed tomography. *JoVE (Journal of Visualized Experiments)* **2018**, *9*, e58501. doi:10.3791/58501.
14. Zhang, Y.; Du, J.; Wang, J.; Ma, L.; Lu, X.; Pan, X.; Guo, X.; Zhao, C. High-throughput micro-phenotyping measurements applied to assess stalk lodging in maize (Zea mays L.). *Biological Research* **2018**, *51*. doi:10.1186/s40659-018-0190-7.
15. Clearwater, M.; Clark, C. In vivo magnetic resonance imaging of xylem vessel contents in woody lianas. *Plant, Cell & Environment* **2003**, *26*, 1205–1214. doi:10.1046/j.1365-3040.2003.01042.x.
16. Van de Wal, B.A.; Windt, C.W.; Leroux, O.; Steppe, K. Heat girdling does not affect xylem integrity: an in vivo magnetic resonance imaging study in the tomato peduncle. *New Phytologist* **2017**, *215*, 558–568. doi:doi.org/10.1111/nph.14610.
17. Scheenen, T.; Heemskerk, A.; De Jager, A.; Vergeldt, F.; Van As, H. Functional imaging of plants: a nuclear magnetic resonance study of a cucumber plant. *Biophysical Journal* **2002**, *82*, 481–492. doi:10.1016/S0006-3495(02)75413-1.
18. Hwang, B.G.; Ryu, J.; Lee, S.J. Vulnerability of protoxylem and metaxylem vessels to embolisms and radial refilling in a vascular bundle of maize leaves. *Frontiers in Plant Science* **2016**, *7*, 941. doi:10.3389/fpls.2016.00941.
19. Zhang, Y.; Ma, L.; Wang, J.; Wang, X.; Guo, X.; Du, J. Phenotyping analysis of maize stem using micro-computed tomography at the elongation and tasseling stages. *Plant methods* **2020**, *16*, 1–14. doi:10.1186/s13007-019-0549-y.
20. Anselmucci, F.; Andò, E.; Viggiani, G.; Lenoir, N.; Arson, C.; Sibille, L. Imaging local soil kinematics during the first days of maize root growth in sand. *Scientific reports* **2021**, *11*, 1–13. doi:10.1038/s41598-021-01056-1.
21. Vita, R.S.; Menezes, N.L.; Pellegrini, M.O.; Melo-de Pinna, G.F. A new interpretation on vascular architecture of the cauline system in Commelinaceae (Commelinales). *Plos one* **2019**, *14*, e0218383. doi:10.1371/journal.pone.0218383.
22. Loepfe, L.; Martinez-Vilalta, J.; Piñol, J.; Mencuccini, M. The relevance of xylem network structure for plant hydraulic efficiency and safety. *Journal of Theoretical Biology* **2007**, *247*, 788–803. doi:10.1016/j.jtbi.2007.03.036.
23. Jahnke, S.; Menzel, M.I.; Van Dusschoten, D.; Roeb, G.W.; Bühler, J.; Minwuyelet, S.; Blümler, P.; Temperton, V.M.; Hombach, T.; Streun, M.; et al. Combined MRI–PET dissects dynamic changes in plant structures and functions. *The Plant Journal* **2009**, *59*, 634–644. doi:10.1111/j.1365-313X.2009.03888.x.
24. Wang, X.; Guan, H.; Huo, Z.; Guo, P.; Du, J.; Wang, W. Maize transpiration and water productivity of two irrigated fields with varying groundwater depths in an arid area. *Agricultural and Forest Meteorology* **2020**, *281*, 107849. doi:10.1016/j.agrformet.2019.107849.
25. Yang, C.T.; Padmanabhan, P.; Gulyás, B.Z. Gadolinium (iii) based nanoparticles for T1-weighted magnetic resonance imaging probes. *RSC advances* **2016**, *6*, 60945–60966. doi:10.1039/c6ra07782j.
26. Cao, Y.; Xu, L.; Kuang, Y.; Xiong, D.; Pei, R. Gadolinium-based nanoscale MRI contrast agents for tumor imaging. *Journal of Materials Chemistry B* **2017**, *5*, 3431–3461. doi:10.1039/C7TB00382J.
27. Gussoni, M.; Greco, F.; Vezzoli, A.; Paleari, M.A.; Moretti, V.M.; Lanza, B.; Zetta, L. Osmotic and aging effects in caviar oocytes throughout water and lipid changes assessed by 1H NMR T1 and T2 relaxation and MRI. *Magnetic Resonance Imaging* **2007**, *25*, 117–128. doi:10.1016/j.mri.2006.08.017.
28. Snaar, J.; Van As, H. Probing water compartments and membrane permeability in plant cells by 1H NMR relaxation measurements. *Biophysical Journal* **1992**, *63*, 1654–1658. doi:10.1016/S0006-3495(92)81741-1.
29. Xin, Y.; Zhang, M.; Adhikari, B. Effect of trehalose and ultrasound-assisted osmotic dehydration on the state of water and glass transition temperature of broccoli (Brassica oleracea L. var. botrytis L.). *Journal of Food Engineering* **2013**, *119*, 640–647. doi:10.1016/j.jfoodeng.2013.06.035.
30. Comtet, J.; Jensen, K.H.; Turgeon, R.; Stroock, A.D.; Hosoi, A. Passive phloem loading and long-distance transport in a synthetic tree-on-a-chip. *Nature Plants* **2017**, *3*, 1–8. doi:10.1038/nplants.2017.32.
31. Min, X.; Kim, W.S. Artificial Xylem Chip: A Three-Dimensionally Printed Vertical Digital Microfluidic Platform. *Langmuir* **2020**, *36*, 14841–14848. doi:10.1021/acs.langmuir.0c02868.

Preprints (www.preprints.org) | NOT PEER-REVIEWED | Posted: 9 May 2022 doi:10.20944/preprints202205.0096.v1

32. Shi, W.; Dalrymple, R.M.; McKenny, C.J.; Morrow, D.S.; Rashed, Z.T.; Surinach, D.A.; Boreyko, J.B. Passive water ascent in a tall, scalable synthetic tree. *Scientific reports* **2020**, *10*, 1–9. doi:10.1038/s41598-019-57109-z.
33. Lee, M.; Lim, H.; Lee, J. Fabrication of artificial leaf to develop fluid pump driven by surface tension and evaporation. *Scientific reports* **2017**, *7*, 1–8. doi:10.1038/s41598-017-15275-y.
34. de Araujo, D.S.; de Moraes, D.H.M.; Mesquita, M.; Flores, R.A.; Battisti, R.; Santos, G.G.; de Deus, F.P.; Ferrarezi, R.S. Numerical Modeling of Microfluid Dynamics in Xylem Vessels of Khaya grandifoliola. *Water* **2021**, *13*, 2723. doi:10.3390/w13192723.
35. Kravtsova, A.; Ianko, P.; Meshalkin, Y.; Bilsky, A. Influence of external periodic perturbation on the flow in T-microchannel. *AIP Conference Proceedings* **2018**, *2027*, 040084. doi:10.1063/1.5065358.
36. Callaghan, P.T. *Principles of nuclear magnetic resonance microscopy*; Oxford University Press on Demand, 1993.
37. Edzes, H.T.; Van Dusschoten, D.; Van As, H. Quantitative T2 imaging of plant tissues by means of multi-echo MRI microscopy. *Magnetic resonance imaging* **1998**, *16*, 185–196. doi:10.1016/S0730-725X(97)00274-9.
38. Köckenberger, W.; Pope, J.; Xia, Y.; Jeffrey, K.; Komor, E.; Callaghan, P. A non-invasive measurement of phloem and xylem water flow in castor bean seedlings by nuclear magnetic resonance microimaging. *Planta* **1997**, *201*, 53–63. doi:10.1007/BF01258680.
39. Rokitta, M.; Peuke, A.; Zimmermann, U.; Haase, A. Dynamic studies of phloem and xylein flow in fully differentiated plants by fast nuclear-magnetic-resonance microimaging. *Protoplasma* **1999**, *209*, 126–131. doi:10.1007/BF01415708.
40. Nikolaev, S.; Zubairova, U. A computational model of the cereal leaves hydraulics. *Journal of Physics: Conference Series* **2021**, *2099*, 012039. doi:10.1088/1742-6596/2099/1/012039.
41. Heinen, R.B.; Ye, Q.; Chaumont, F. Role of aquaporins in leaf physiology. *Journal of experimental botany* **2009**, *60*, 2971–2985. doi:10.1093/jxb/erp171.
42. Wheeler, T.D.; Stroock, A.D. The transpiration of water at negative pressures in a synthetic tree. *Nature* **2008**, *455*, 208–212. doi:10.1038/nature07226.
43. Noblin, X.; Mahadevan, L.; Coomaraswamy, I.; Weitz, D.A.; Holbrook, N.M.; Zwieniecki, M.A. Optimal vein density in artificial and real leaves. *Proceedings of the National Academy of Sciences* **2008**, *105*, 9140–9144. doi:10.1073/pnas.0709194105.
44. Hoffmann, M.; Schlüter, M.; Räbiger, N. Experimental investigation of liquid–liquid mixing in T-shaped micro-mixers using μ-LIF and μ-PIV. *Chemical engineering science* **2006**, *61*, 2968–2976. doi:10.1016/j.ces.2005.11.029.
45. Silva, G.; Leal, N.; Semiao, V. Micro-PIV and CFD characterization of flows in a microchannel: velocity profiles, surface roughness and Poiseuille numbers. *International Journal of Heat and Fluid Flow* **2008**, *29*, 1211–1220. doi:10.1016/j.ijheatfluidflow.2008.03.013.
46. Thomas, S.; Ameel, T.A. An experimental investigation of moderate Reynolds number flow in a T-Channel. *Experiments in fluids* **2010**, *49*, 1231–1245. doi:10.1007/s00348-010-0863-7.
47. Zubairova, U.S.; Verman, P.Y.; Oshchepkova, P.A.; Elsukova, A.S.; Doroshkov, A.V. LSM-W 2: laser scanning microscopy worker for wheat leaf surface morphology. *BMC systems biology* **2019**, *13*, 33–44. doi:10.1186/s12918-019-0689-8.
48. Legland, D.; Arganda-Carreras, I.; Andrey, P. MorphoLibJ: integrated library and plugins for mathematical morphology with ImageJ. *Bioinformatics* **2016**, *32*, 3532–3534. doi:10.1093/bioinformatics/btw413.
49. Raju, C.S.K.; Cossmer, A.; Scharf, H.; Panne, U.; Lück, D. Speciation of gadolinium based MRI contrast agents in environmental water samples using hydrophilic interaction chromatography hyphenated with inductively coupled plasma mass spectrometry. *Journal of analytical atomic spectrometry* **2010**, *25*, 55–61. doi:10.1039/B919959D.
50. Kravtsova, A.Y. Visualization of Flow Regimes in Symmetric Microchannel in Case of Different Inlet Flowrate Ratios for Fixed Outlet Reynolds Number. *Journal of Engineering Thermophysics* **2020**, *29*, 612–617. doi:10.1134/S1810232820040098.
51. Kravtsova, A.Y.; Markovich, D.; Pervunin, K.; Timoshevskiy, M.; Hanjalić, K. High-speed visualization and PIV measurements of cavitating flows around a semi-circular leading-edge flat plate and NACA0015 hydrofoil. *International Journal of Multiphase Flow* **2014**, *60*, 119–134. doi:10.1016/j.ijmultiphaseflow.2013.12.004.